Supplement of Earth Surf. Dynam., 12, 181–199, 2024
https://doi.org/10.5194/esurf-12-181-2024-supplement

Earth Surface Dynamics
Open Access
EGU

Supplement of

Statistical characterization of erosion and sediment transport mechanics in shallow tidal environments – Part 1: Erosion dynamics

Andrea D'Alpaos et al.

Correspondence to: Davide Tognin (davide.tognin@unipd.it)

Supplement

1 The Wind-Wave-Tidal Model

1.1 Hydrodynamic model

The hydrodynamic module solves the 2D depth-integrated shallow water equations, phase averaged over a representative elementary area in order to deal with wetting and drying processes in very shallow and irregular domains (Defina, 2000):

$$\vartheta(\eta)\frac{\partial \eta}{\partial t} + \nabla \cdot \boldsymbol{q} = 0 \tag{1}$$

$$\frac{D}{Dt}\left(\frac{\boldsymbol{q}}{Y}\right) + \frac{1}{Y}\nabla \cdot \boldsymbol{Re} + \frac{\boldsymbol{\tau_t}}{\rho Y} - \frac{\boldsymbol{\tau_s}}{\rho Y} + g\nabla h = 0 \tag{2}$$

where t is time, D/Dt is the material time derivative, ∇ and $\nabla\cdot$ denote the 2D gradient and divergence operators, respectively. In the continuity equation (Eq. 1), η is the free surface elevation, ϑ is the wet fraction of the computational domain, which is a function of water depth and local topographic unevenness (Defina, 2000), $\boldsymbol{q} = (q_x, q_y)$ is the depth-integrated velocity (i.e., discharge per unit width). In the momentum equations (Eq. 2), Y is the effective water depth (i.e., the water volume per unit area), $\boldsymbol{\tau_t}$ and $\boldsymbol{\tau_s}$ are the shear stresses at the bottom and at the free surface, respectively, ρ is water and g is gravity acceleration. The Reynolds stresses $\boldsymbol{Re}$ are computed using a depth-averaged version of Smagorinsky's model (Smagorinsky, 1963) and they read:

$$\boldsymbol{Re} = R_{ij} = \nu_e Y(u_{i,j} + u_{j,i}) \tag{3}$$

with i, j denoting either the x or y coordinate, $\boldsymbol{u} = \boldsymbol{q}/Y$ and the eddy viscosity ν_e is computed as

$$\nu_e = 2C_S^2 A_e \sqrt{2(u_{x,x})^2 + (u_{x,y} + u_{y,x})^2 + 2(u_{y,y})^2} \tag{4}$$

where the Smagorinsky coefficient C_S is set equal to 0.2 and A_e is the area of the computational element.

In the numerical scheme, the material time derivative in Eq. 2 is solved with the method of characteristics by expressing it as the finite difference in time. This allows solving the continuity equation (Eq. 1) with a semi-implicit scheme, resulting in a self-adjoint spatial operator, which is solved on a staggered triangular grid with the finite element method of Galerkin and flow rates are obtained by back substitution.

1.2 Wind wave model

The wind-wave module (Carniello et al., 2011) solves the wave action conservation equation using the same computational grid of the hydrodynamic module, which provides water depths and depth-averaged flow velocities, used to propagate the wind-wave field. In the frequency domain, the wave action density, N_0, evolves according to (Carniello et al., 2005)

$$\frac{\partial N_0}{\partial t} + \frac{\partial}{\partial x} c'_{gx} N_0 + \frac{\partial}{\partial y} c'_{gy} N_0 = S_0 \tag{5}$$

where c'_{gx} and c'_{gy} are the wave group celerity components used to approximate the speed propagation of N_0 (Holthuijsen et al., 1989), S_0 denotes the wind-wave source terms, accounting both for positive (wind energy input) and negative (bottom friction, whitecapping, and depth-induced breaking) contributions.

The wave-action conservation equation (Eq. 5) is solved with an upwind finite volume scheme based on the same computational grid of the hydrodynamic model. In each element at each time step, the wind-wave model computes the wave action, from which the significant wave height is obtained by applying the linear theory.

1.3 Model calibration

The calibration of the model was performed for different periods, but here we focus as an example on the period 8-13 November 2004, for which not only water levels, but also flow rates at the inlets are available. This period was initially characterized by quite low wind speeds (U_{wind} =7.0 m/s between 8 and 10 November) followed by an intense Bora event with wind speeds up to 18 m/s (Figure S2). Model capability to capture the process is evaluated by means of the Nash-Sutcliffe Model Efficiency (NSE) (Allen et al., 2007). Figure S2 shows the comparison between measured and computed water levels at three tide-gauge stations: Pagliaga, Punta della Salute and Brondolo, located in the northern, central and southern portions of the lagoon, respectively. The comparison highlights a very good agreement between computed and measured water levels (NSE_{mean} = 0.970, NSE_{median} = 0.984, NSE_{std} = 0.040) Figure S3 compares computed and measured flow rates at the three inlets in the same period. The comparison is quite favourable (NSE_{mean} = 0.853, NSE_{median} = 0.931, NSE_{std} = 0.184) and only when the wind speed reaches the highest value of about 18 m/s the model slightly underestimates the maximum water discharge. The wind-wave measurements within the Venice lagoon were performed only in 2002 and 2003, therefore, we focus as an example on the period 11-14 February 2003. Figures S4 and S5 show the comparison between measured and computed wave peak periods and wave heights, respectively, at the 1BF station, located in the northern lagoon, and the 2BF station located in the central lagoon (see Carniello et al. (2011) for the location of the stations). The comparison between measured and computed wave heights and periods confirms the capability of the coupled WWTM to reproduce the modulation of the wave height induced by water-level oscillations and wind-speed variations (NSE_{mean} = 0.627, NSE_{median} = 0.756, NSE_{std} = 0.357). In particular, Figure S4 shows

the effectiveness of the suggested empirical correlation function relating the mean peak wave period to the local wind speed and water depth (Carniello et al., 2011).

2 Boundary conditions selection

To simulate the typical wave-driven BSS conditions in the Venice Lagoon, we carefully analyse the wind climate measured in the period 2000-2020. In particular, we compared the wind velocity measured in each year with that of the whole period 2000-2020 by means of the two-sample Kolmogorov-Smirnov (KS) test and the Wilcoxon (W) test (Table S6). We selected the wind velocity measured in 2005 because it does not significantly differ from that of the whole considered period according to both the KS and W tests. A visual comparison of the cumulative distribution frequency $F(x)$ of wind velocity also confirms this choice (Figure S6).

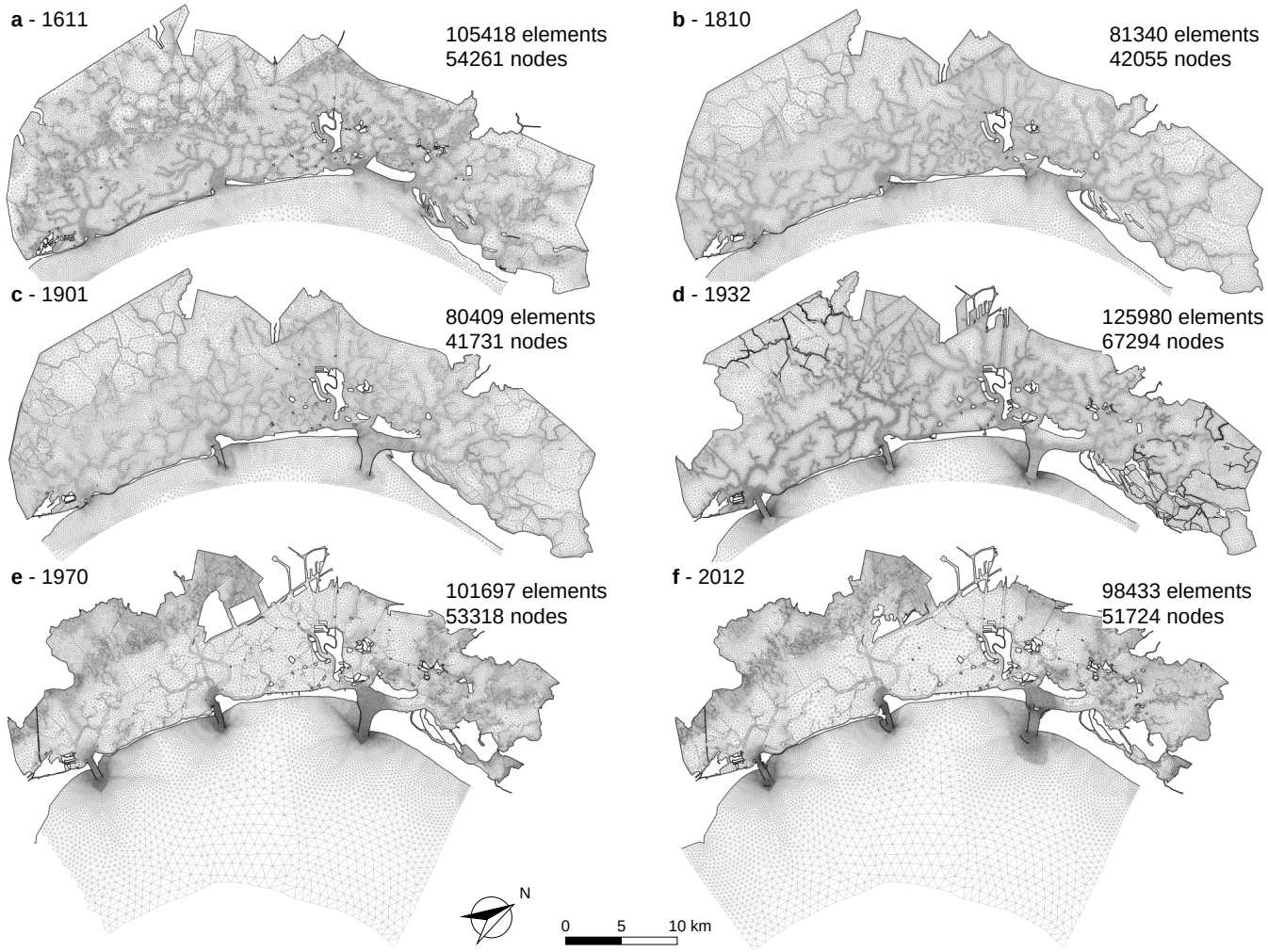

Figure S1. Meshes used in the numerical model. Meshes of the six different configurations of the Venice Lagoon: (**a**) 1611, (**b**) 1810, (**c**) 1901, (**d**) 1932, (**e**) 1970, and (**f**) 2012. For the sake of clarity, the mesh portion representing the sea is shown only in panel (**e**) and (**f**), but it is present in all meshes.

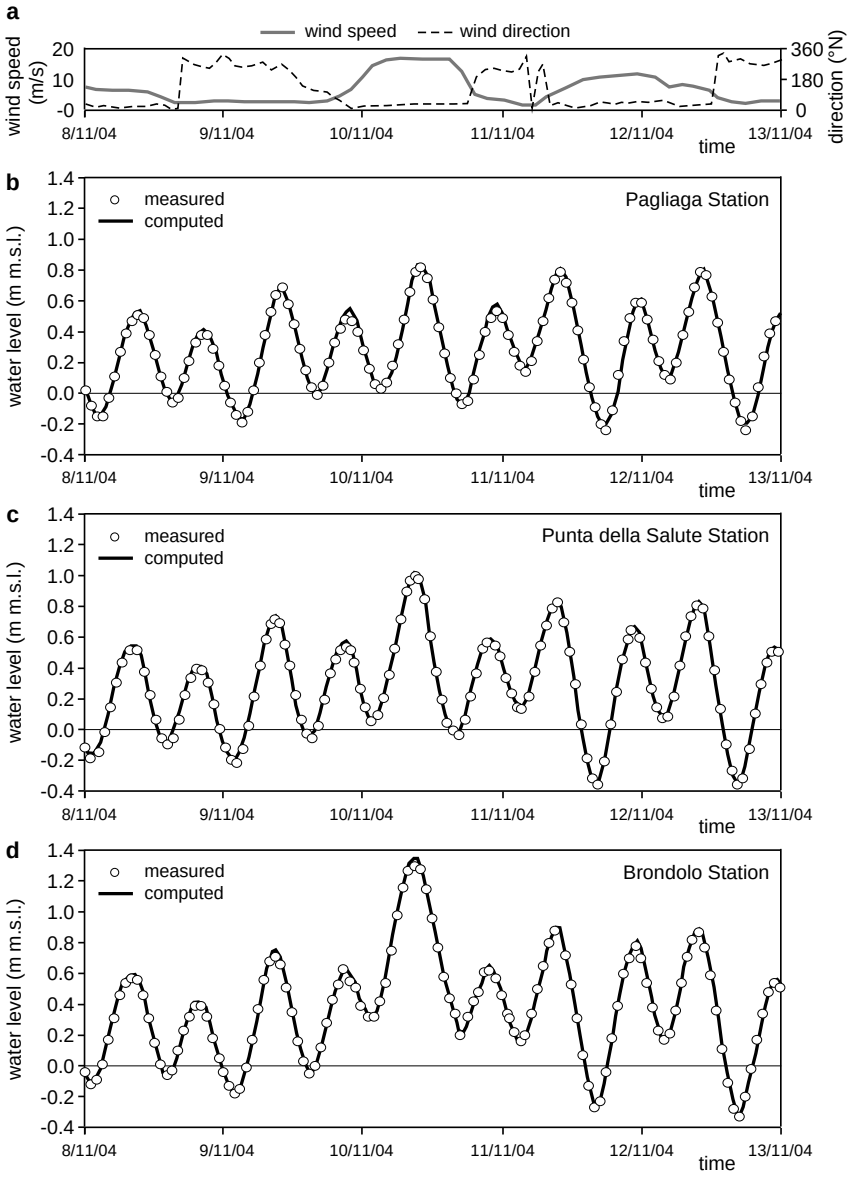

Figure S2. Model calibration: water level. Comparison between observations and model results for the period 8-13 November 2004: (**a**) Measured wind speed and direction; comparison of measured (circles) and computed (solid lines) water levels at the Pagliaga (**b**); at the Punta della Salute (**c**); and at the Brondolo station (**d**) (adapted from Carniello et al., 2011).

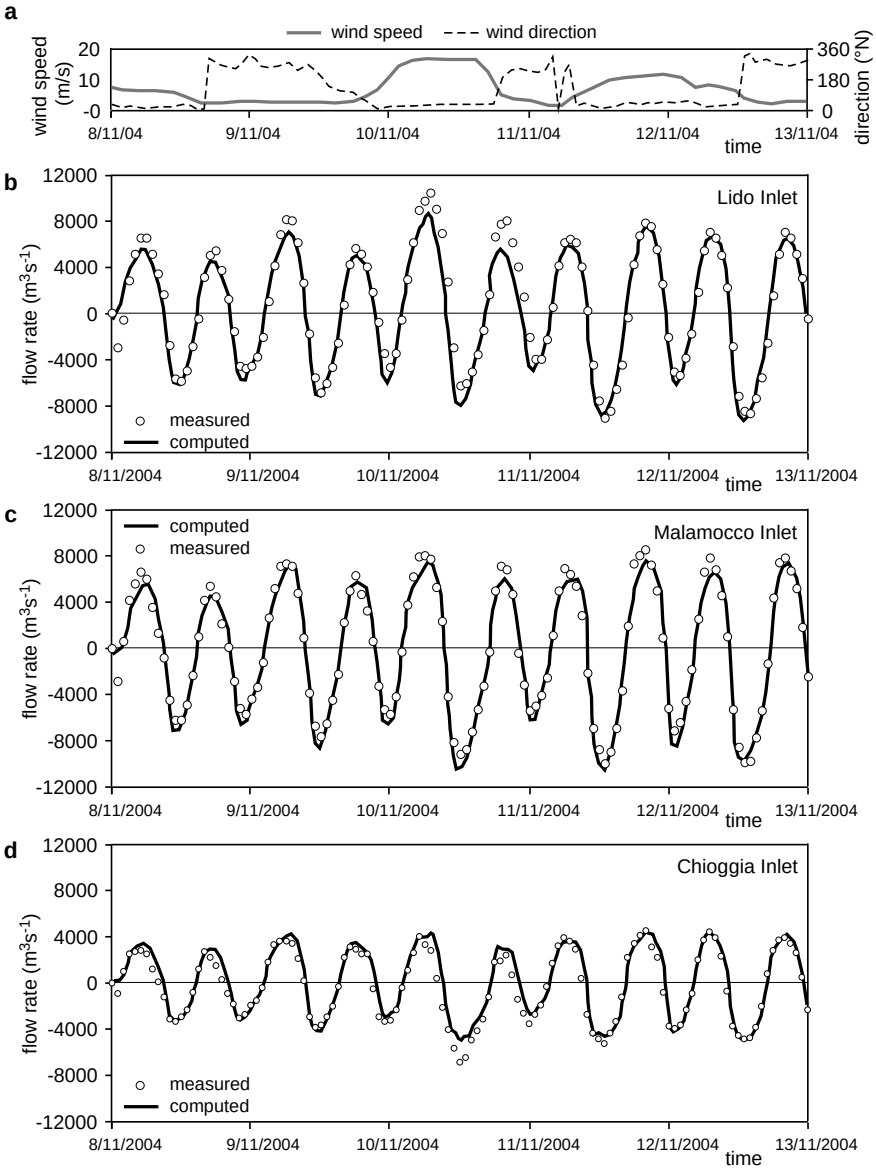

Figure S3. Model calibration: flow rate. Comparison between observations and model results for the period 8-13 November 2004: (**a**) Measured wind speed and direction; comparison of measured (circles) and computed (solid lines) water discharges at the Lido Inlet (**b**); at the Malamocco Inlet (**c**); and at the Chioggia Inlet (**d**). Positive values refer to the food phase, negative values to the ebb phase (adapted from Carniello et al., 2011).

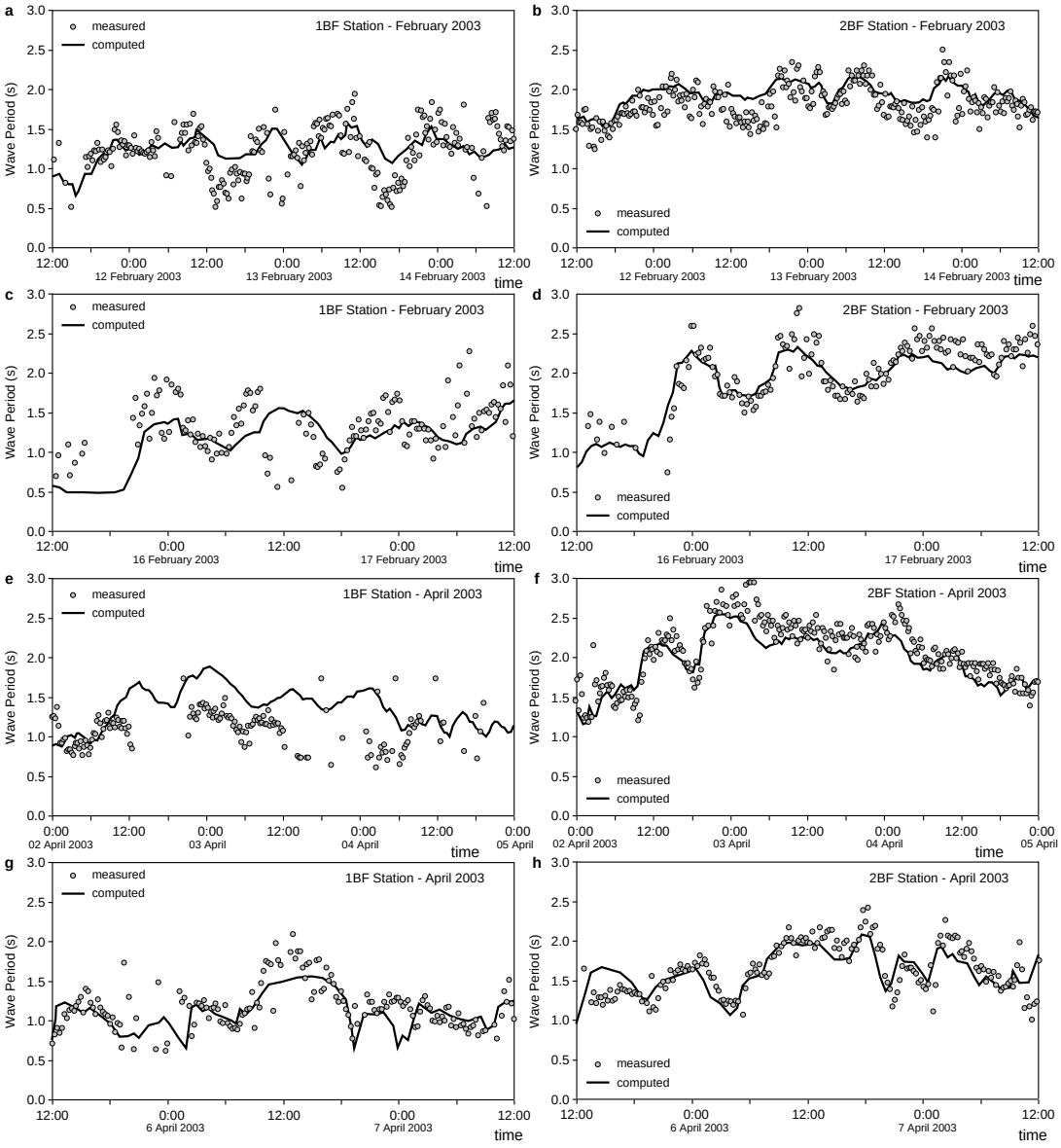

Figure S4. Model calibration: wave peak period. Comparison of measured (circles) and computed (solid lines) wave peak period at the 1BF station (**a, c, e, g**) and 2BF station (**b, d, f, h**) (adapted from Carniello et al., 2011).

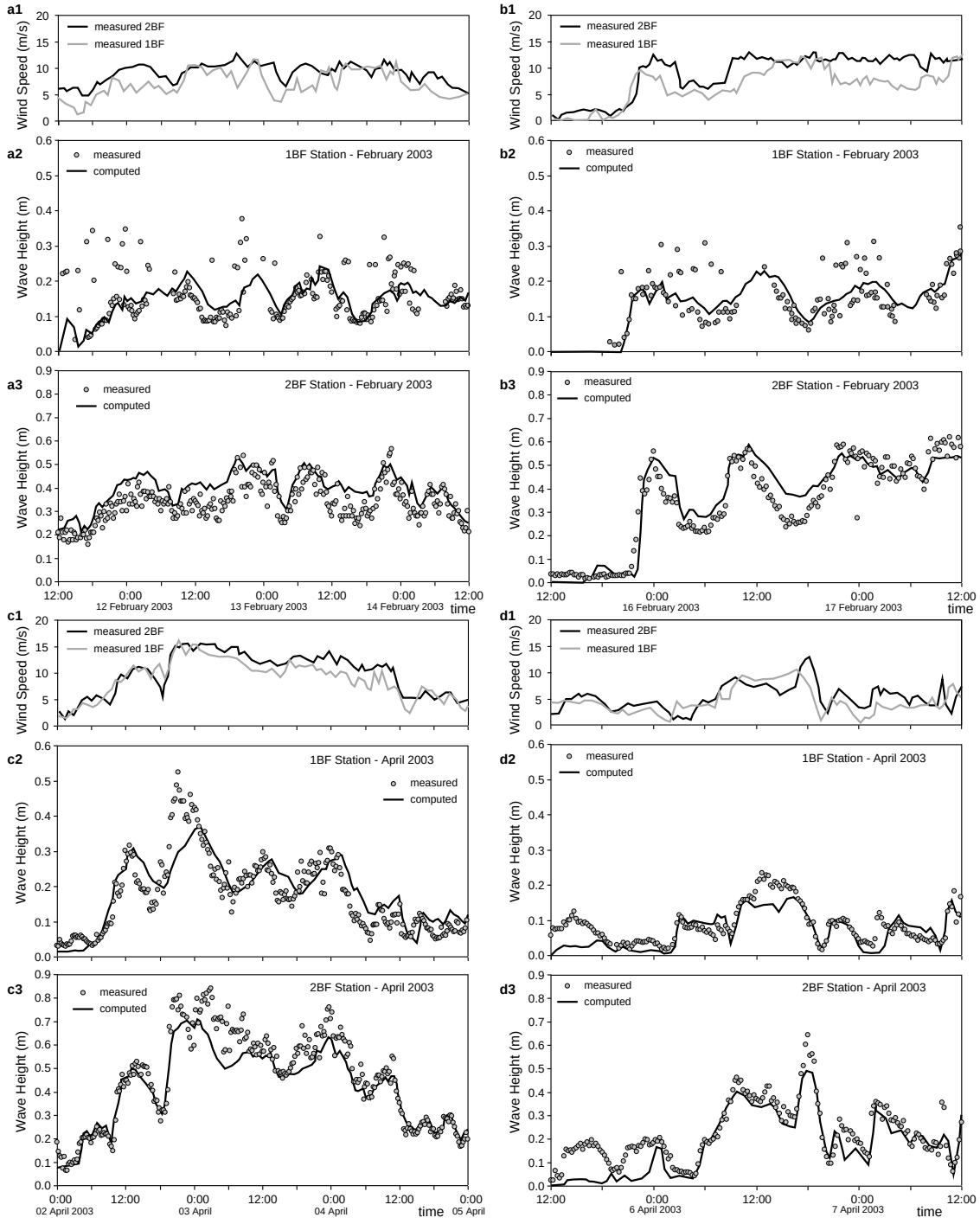

Figure S5. Model calibration: wave height. Comparison of measured (circles) and computed (solid lines) wave heights at the 1BF station (**a2, b2, c2, d2**) and 2BF station (**a3, b3, c3, d3**) (adapted from Carniello et al., 2011).

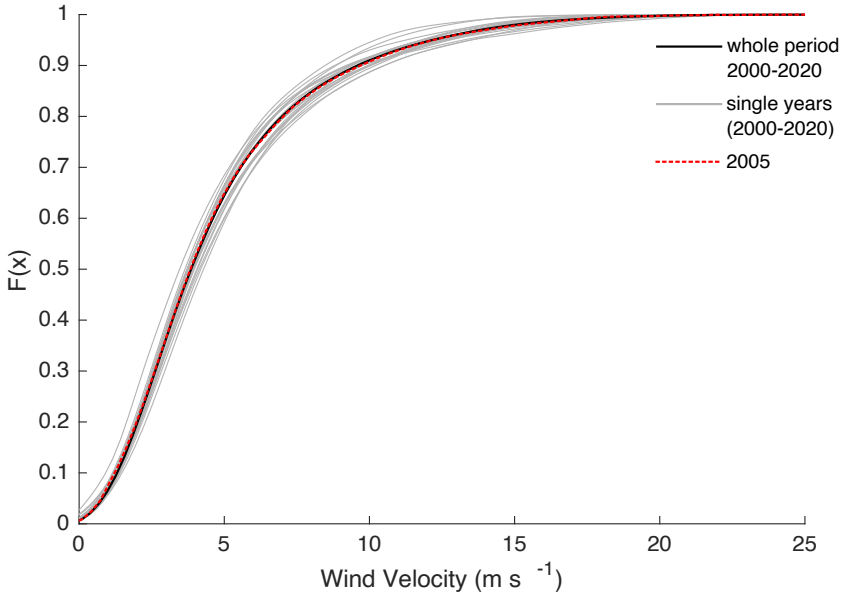

Figure S6. Wind climate for the period 2000-2020. Cumulative density function $F(x)$ of wind velocity for the period 2000-2020. Grey lines represent $F(x)$ of every single year, the red dashed line is the year 2005, and the black thick line represents the whole period 2000-2020.

Table S1. Results of the Kolmogorv-Smirnov (KS) and Wilcoxon (W) tests on wind velocity.

Year	KS test		W test	
	$p-$value	h	$p-$value	h
2000	< 0.001	1	< 0.001	1
2001	< 0.001	1	< 0.001	1
2002	< 0.001	1	< 0.001	1
2003	< 0.001	1	< 0.001	1
2004	< 0.001	1	0.024	1
2005	0.072	0	0.283	0
2006	< 0.001	1	< 0.001	1
2007	0.002	1	0.712	0
2008	< 0.001	1	< 0.001	1
2009	0.002	1	0.006	1
2010	< 0.001	1	< 0.001	1
2011	< 0.001	1	< 0.001	1
2012	< 0.001	1	< 0.001	1
2013	< 0.001	1	< 0.001	1
2014	< 0.001	1	0.003	1
2015	< 0.001	1	0.020	1
2016	< 0.001	1	0.055	0
2017	< 0.001	1	0.033	1
2018	< 0.001	1	< 0.001	1
2019	< 0.001	1	< 0.001	1
2020	< 0.001	1	< 0.001	1

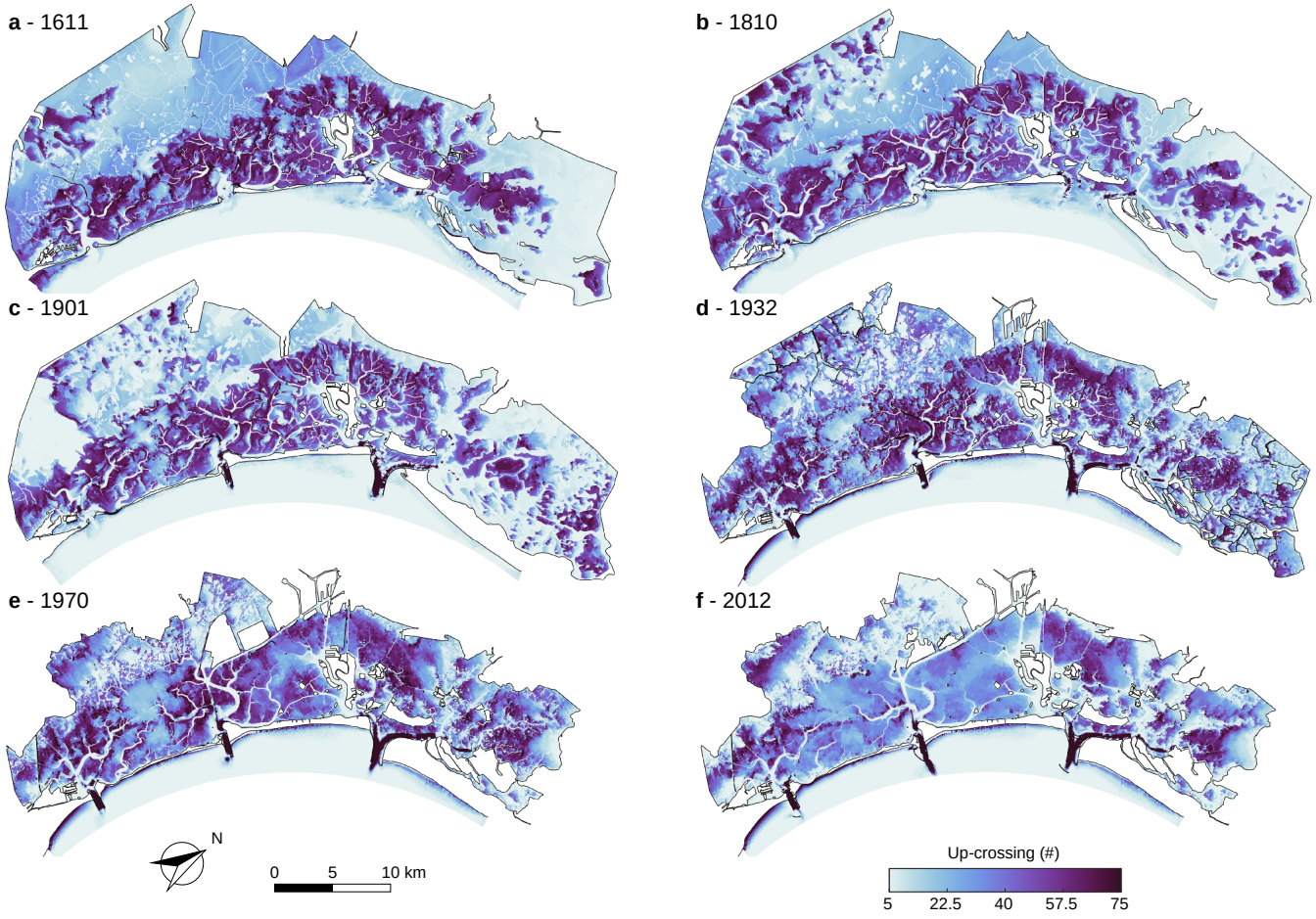

Figure S7. Number of upcrossings of the erosion threshold. Spatial distribution of the number of upcrossings of the threshold for erosion $\tau_c = 0.4$ Pa for the six different configurations of the Venice Lagoon: (**a**) 1611, (**b**) 1810, (**c**) 1901, (**d**) 1932, (**e**) 1970, and (**f**) 2012.

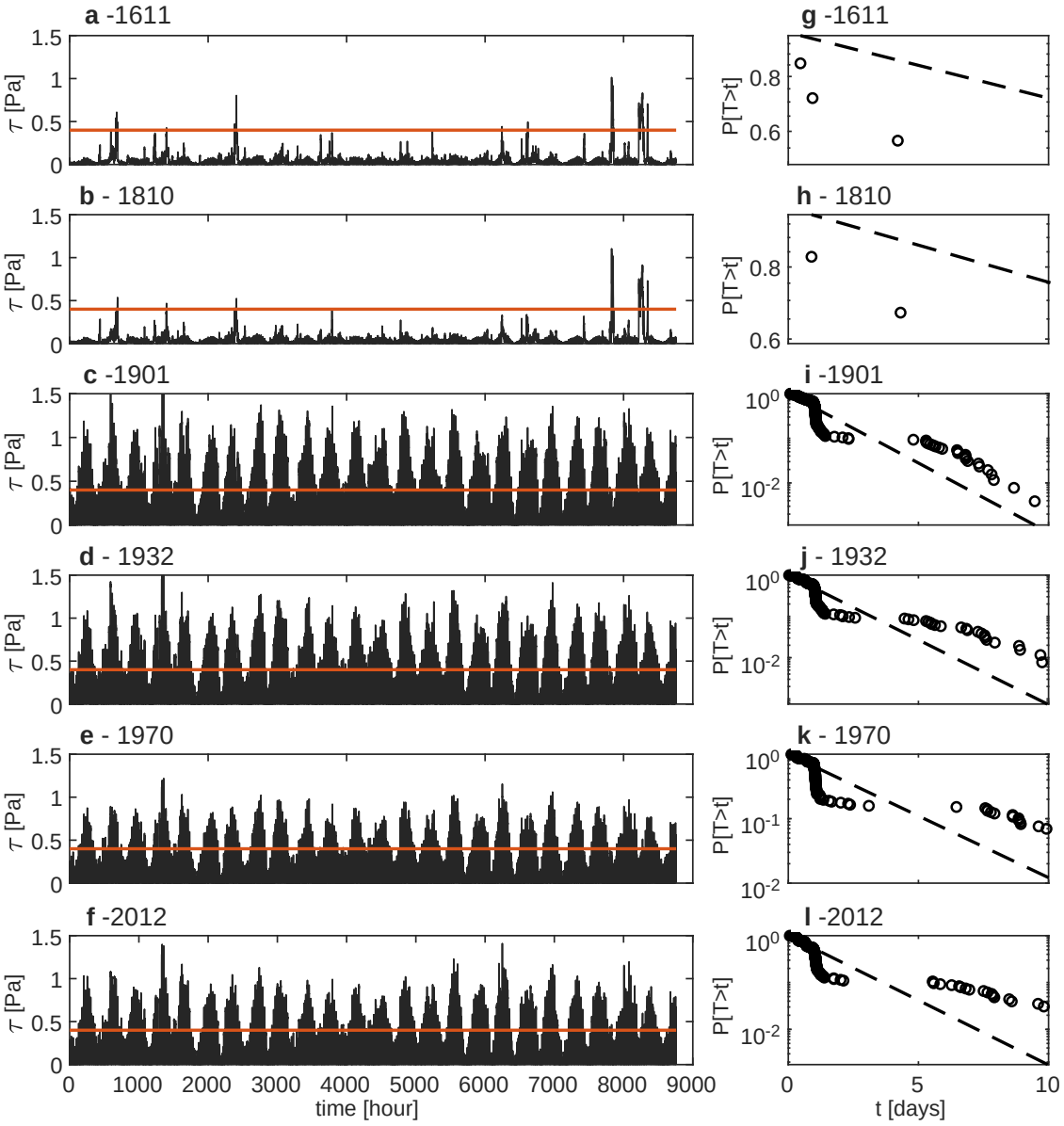

Figure S8. Over-threshold BSS events at the Lido inlet. Statistical analysis at SL station in the Lido inlet: time series of the computed BSS (**a-f**); probability distributions of the interarrival times (circles) and exponential distributions (dashed lines) (**g-l**).

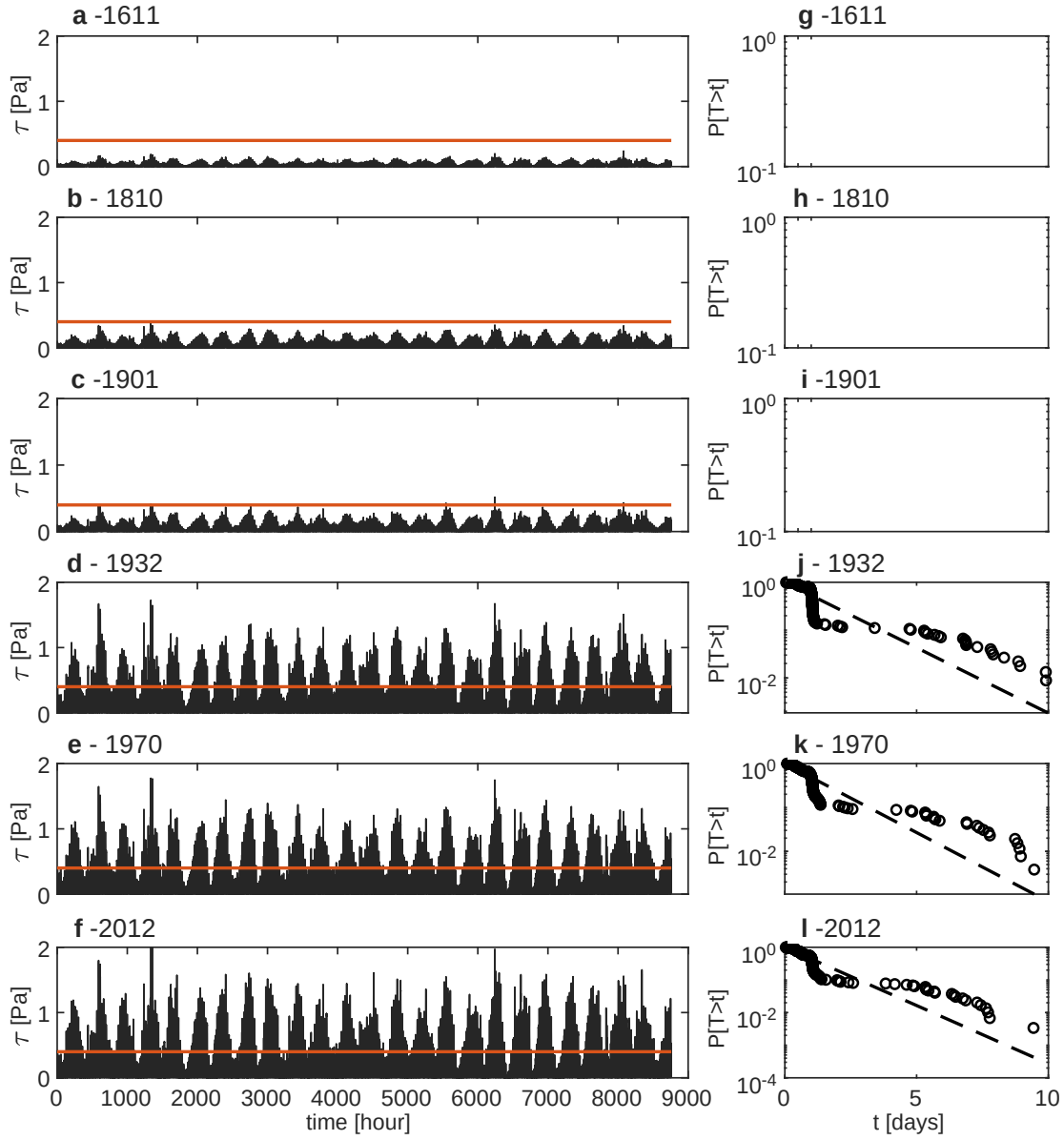

Figure S9. Over-threshold BSS events at the Chioggia inlet. Statistical analysis at SC station in the Chioggia inlet: time series of the computed BSS (**a-f**); probability distributions of the interarrival times (circles) and exponential distributions (dashed lines) (**g-l**).

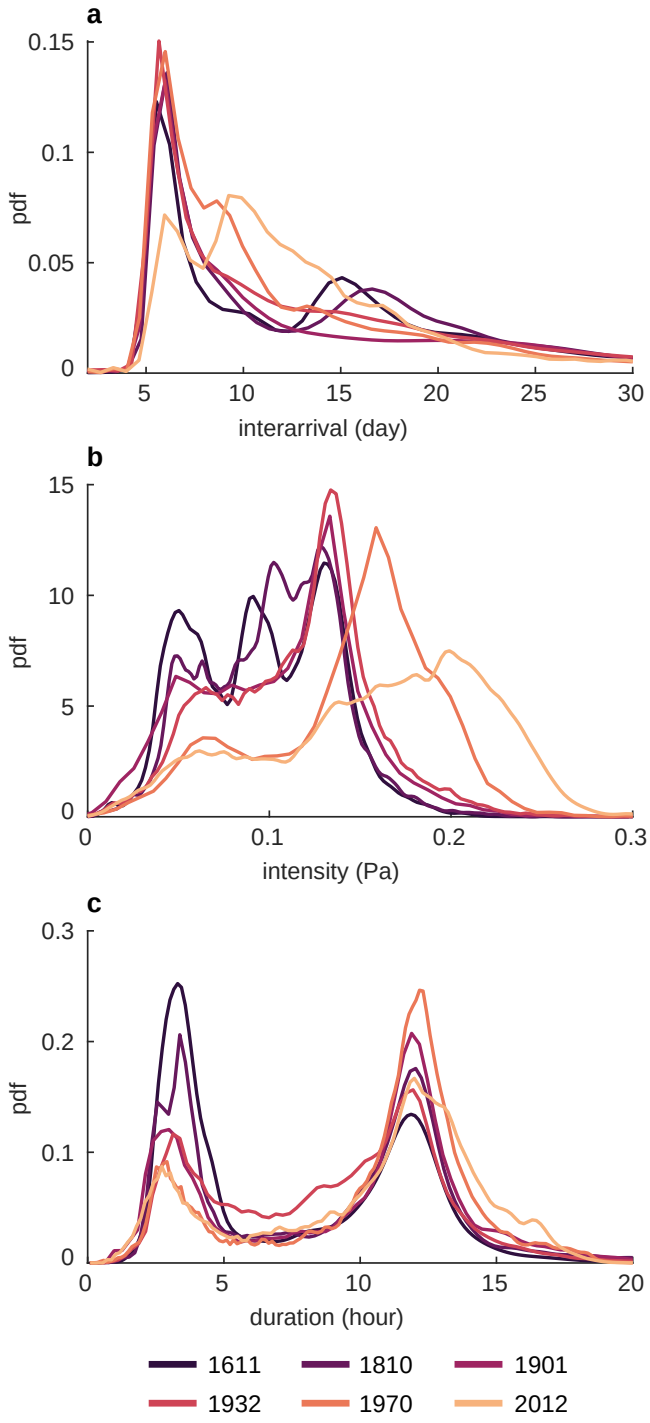

Year	t [day]	
	(mean $\pm$ std)	(median)
1611	45.27 $\pm$ 76.56	16.29
1810	34.30 $\pm$ 61.99	15.69
1901	48.35 $\pm$ 80.10	15.14
1932	26.09 $\pm$ 40.21	13.17
1970	20.35 $\pm$ 32.07	10.07
2012	26.13 $\pm$ 42.83	12.67

Year	e [Pa]	
	(mean $\pm$ std)	(median)
1611	0.09 $\pm$ 0.03	0.09
1810	0.10 $\pm$ 0.03	0.10
1901	0.10 $\pm$ 0.04	0.11
1932	0.11 $\pm$ 0.04	0.12
1970	0.14 $\pm$ 0.04	0.15
2012	0.16 $\pm$ 0.06	0.16

Year	d [hour]	
	(mean $\pm$ std)	(median)
1611	7.54 $\pm$ 4.32	6.47
1810	8.84 $\pm$ 4.76	10.18
1901	9.67 $\pm$ 5.06	11.12
1932	8.95 $\pm$ 4.02	9.75
1970	10.36 $\pm$ 3.92	11.64
2012	10.27 $\pm$ 4.24	11.57

Figure S10. Spatial probability density function of interarrival time, intensity and duration of BSS over-threshold events. Probability density function (left), mean (mean $\pm$ standard deviation) and median value (right) of interarrival times t (**a**), intensity e (**b**) and duration d (**c**) of BSS over-threshold events.

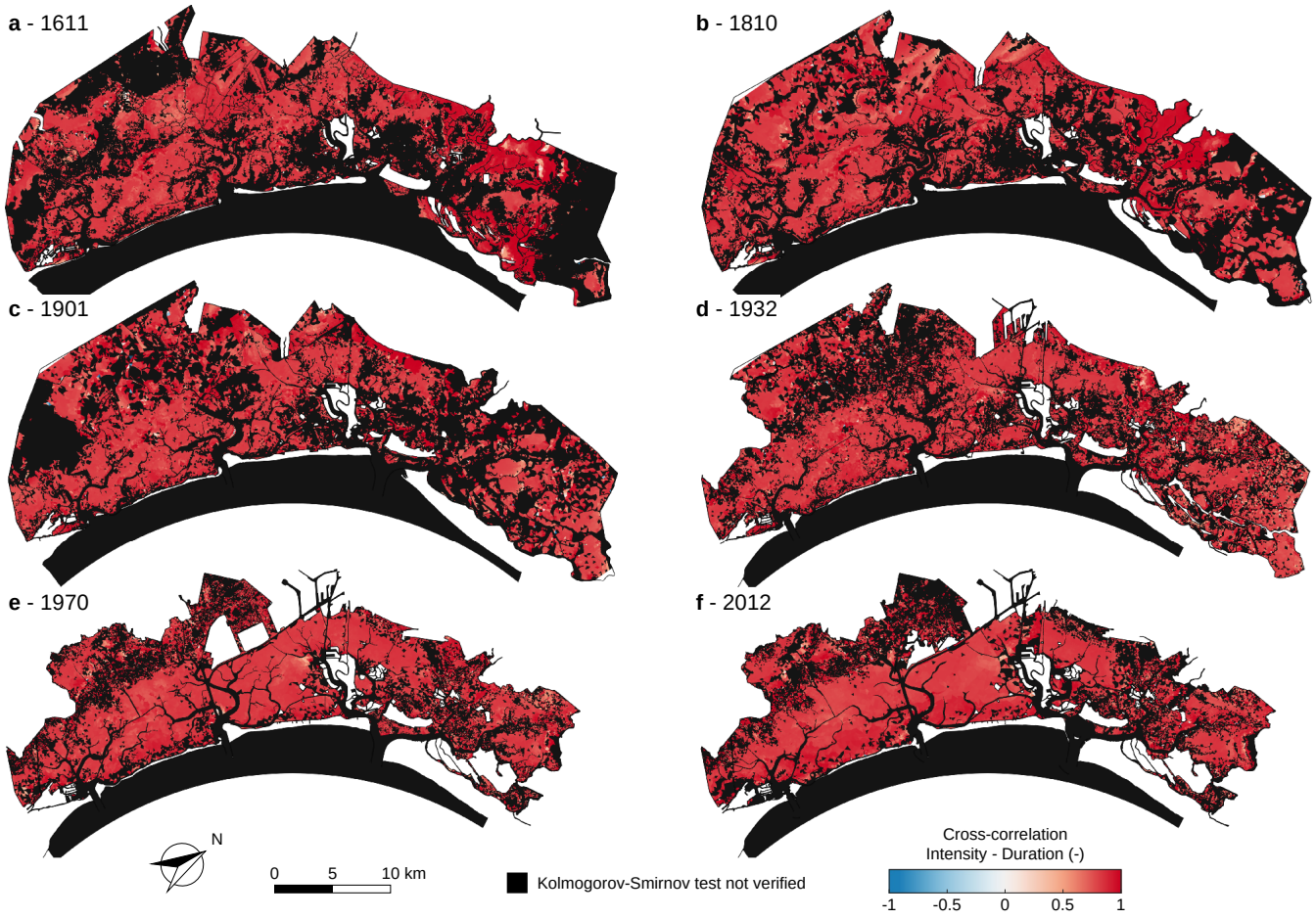

Figure S11. Cross-correlation between intensity and duration of over-threshold BSS events. Spatial distribution of temporal cross-correlation between intensity of peak-excesses and duration of over-threshold exceedances for the six different configurations of the Venice Lagoon: (**a**) 1611, (**b**) 1810, (**c**) 1901, (**d**) 1932, (**e**) 1970, and (**f**) 2012. Black identifies sites where the bottom shear stress cannot be modelled as a marked Poisson process (i.e. the KS test is not verified for the interarrival time).

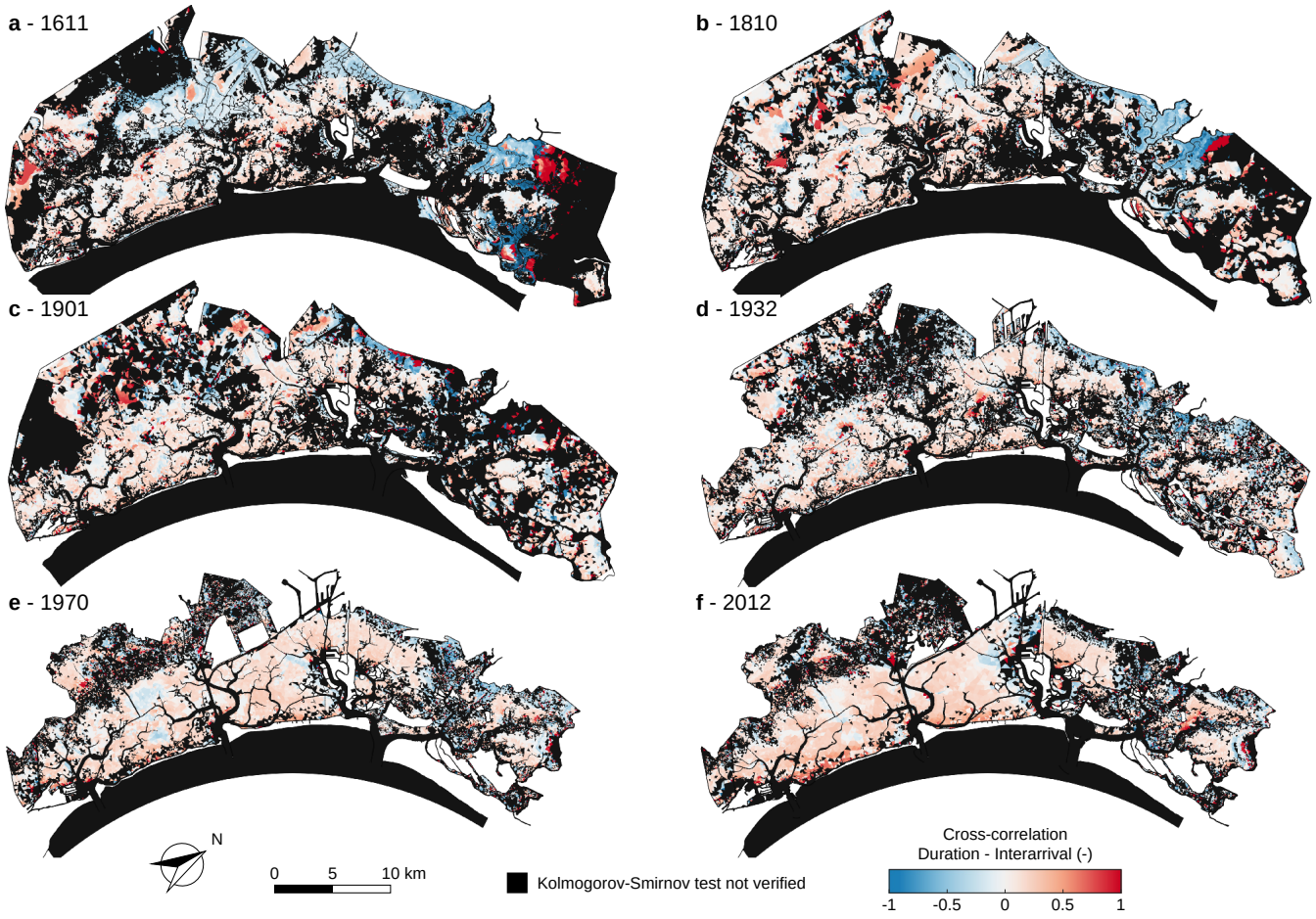

Figure S12. Cross-correlation between duration and interarrival times of over-threshold BSS events. Spatial distribution of temporal cross-correlation between duration and interarrival times of over-threshold exceedances for the six different configurations of the Venice Lagoon: (**a**) 1611, (**b**) 1810, (**c**) 1901, (**d**) 1932, (**e**) 1970, and (**f**) 2012. Black identifies sites where the bottom shear stress cannot be modelled as a marked Poisson process (i.e. the KS test is not verified for the interarrival time).

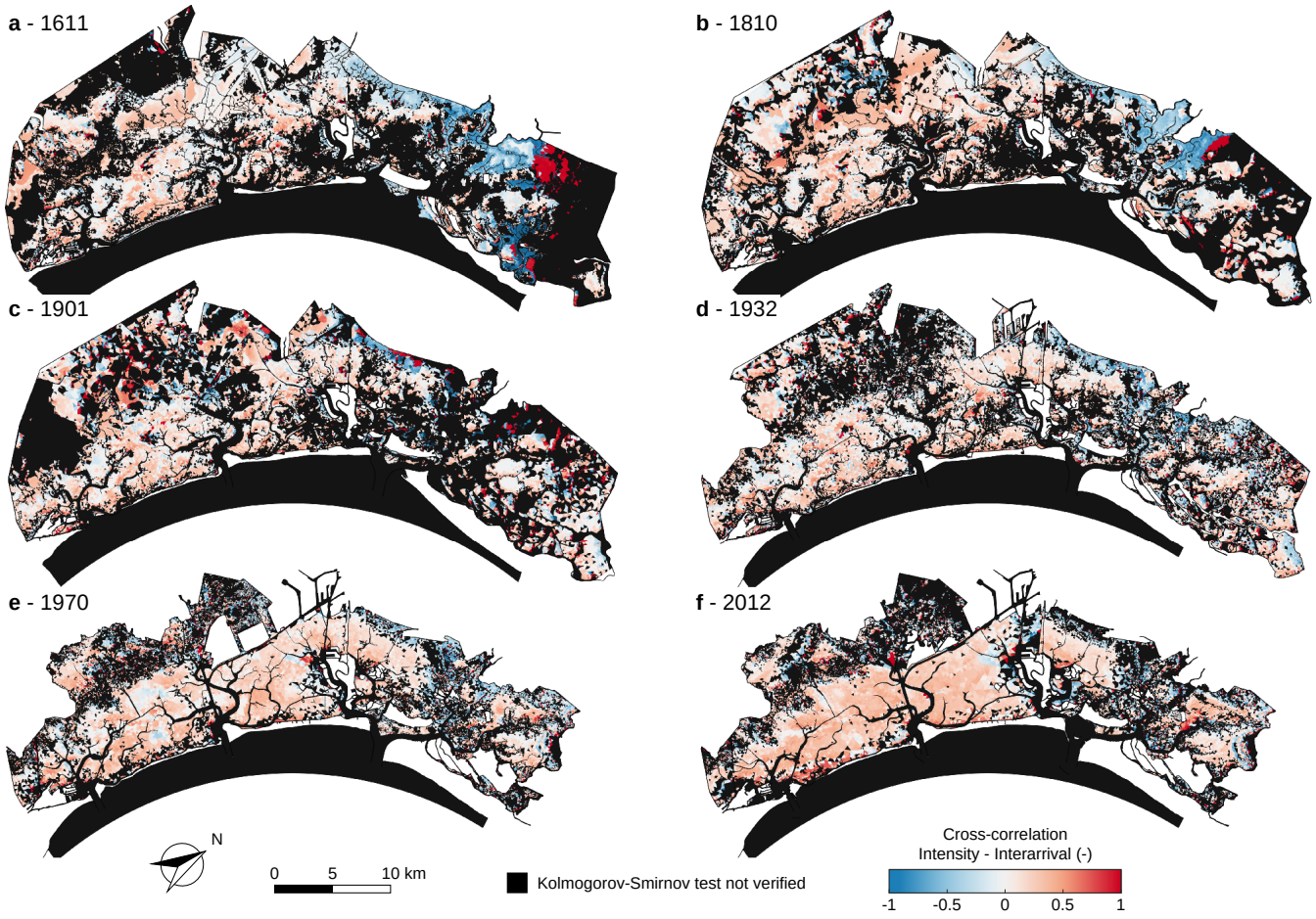

Figure S13. Cross-correlation between intensity and interarrival times of over-threshold BSS events. Spatial distribution of temporal cross-correlation between intensity of peak-excesses and interarrival times of over-threshold exceedances for the six different configurations of the Venice Lagoon: (**a**) 1611, (**b**) 1810, (**c**) 1901, (**d**) 1932, (**e**) 1970, and (**f**) 2012. Black identifies sites where the bottom shear stress cannot be modelled as a marked Poisson process (i.e. the KS test is not verified for the interarrival time) .

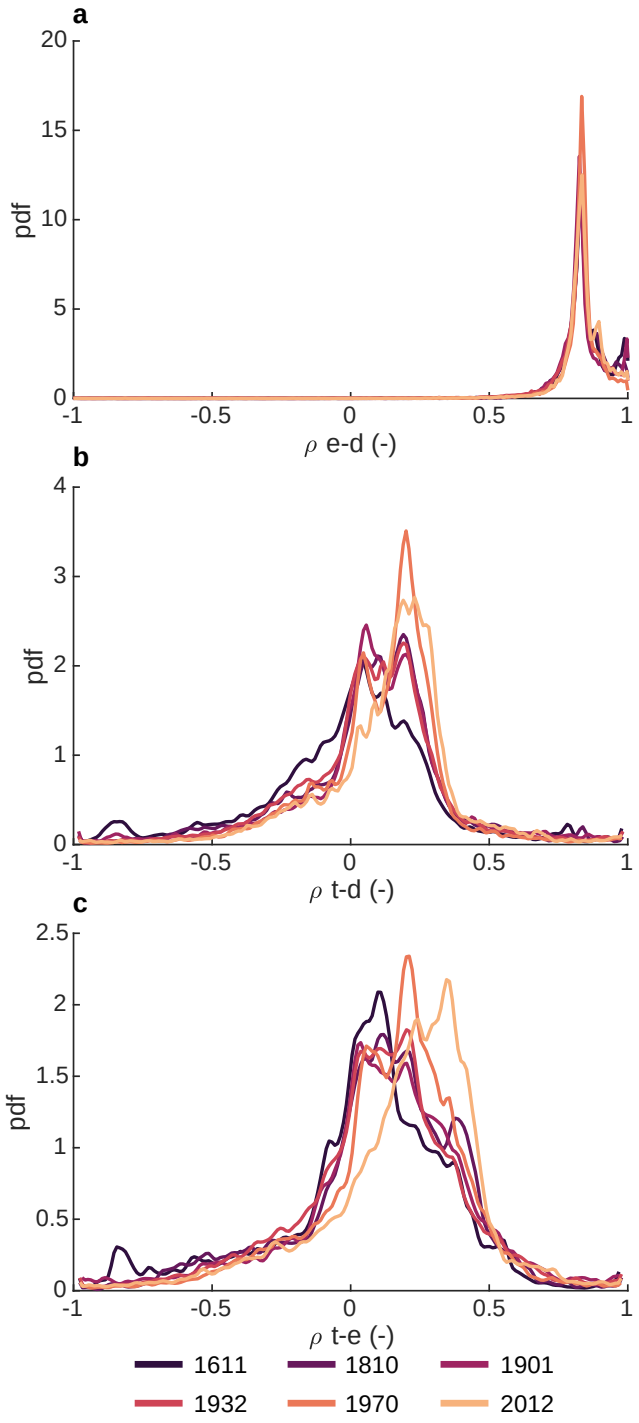

Year	$\rho(e-d)$ [-] (mean $\pm$ std)
1611	0.84 ± 0.09
1810	0.83 ± 0.09
1901	0.82 ± 0.11
1932	0.82 ± 0.11
1970	0.83 ± 0.08
2012	0.83 ± 0.09

Year	$\rho(t-d)$ [-] (mean $\pm$ std)
1611	0.005 ± 0.365
1810	0.069 ± 0.318
1901	0.078 ± 0.356
1932	0.070 ± 0.312
1970	0.105 ± 0.277
2012	0.130 ± 0.308

Year	$\rho(t-e)$ [-] (mean $\pm$ std)
1611	0.05 ± 0.37
1810	0.10 ± 0.33
1901	0.11 ± 0.37
1932	0.10 ± 0.33
1970	0.14 ± 0.30
2012	0.18 ± 0.33

Figure S14. Spatial probability density function of cross-correlation between interarrival time, intensity and duration of BSS over-threshold events. Probability density function (left) and mean value (mean $\pm$ standard deviation, right) of cross-correlation between intesity and duration $\rho(e-d)$ (**a**), interarrival time and duration $\rho(t-d)$ (**b**) and interarrival time and intensity $\rho(t-e)$ (**c**).

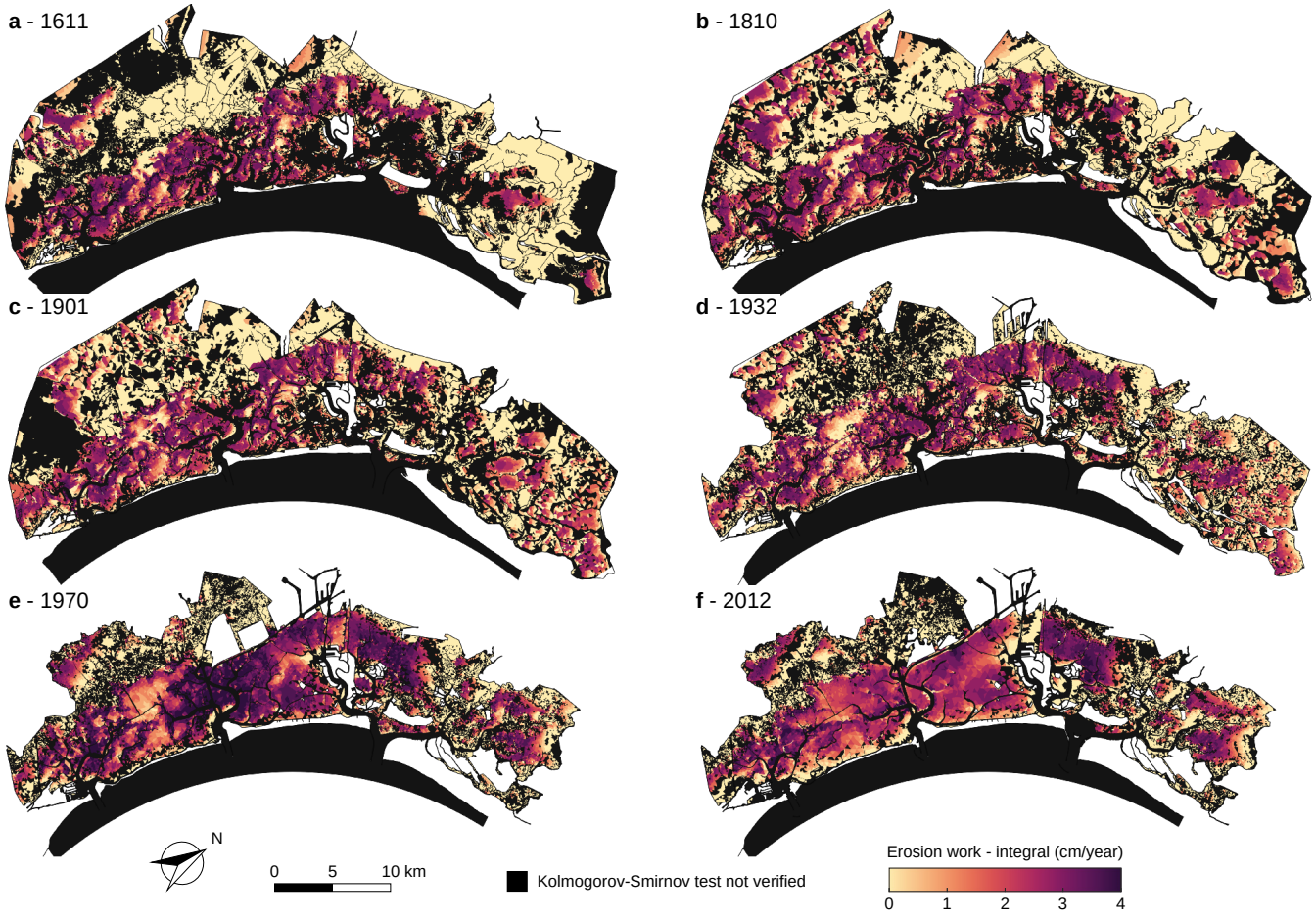

Figure S15. Erosion work computed as integral of over-threshold BSS events. Spatial distribution of erosion work computed with Eq. 2 for the six different configurations of the Venice Lagoon: (**a**) 1611, (**b**) 1810, (**c**) 1901, (**d**) 1932, (**e**) 1970, and (**f**) 2012. Black identifies sites where the bottom shear stress cannot be modelled as a marked Poisson process (i.e. the KS test is not verified for the interarrival time).

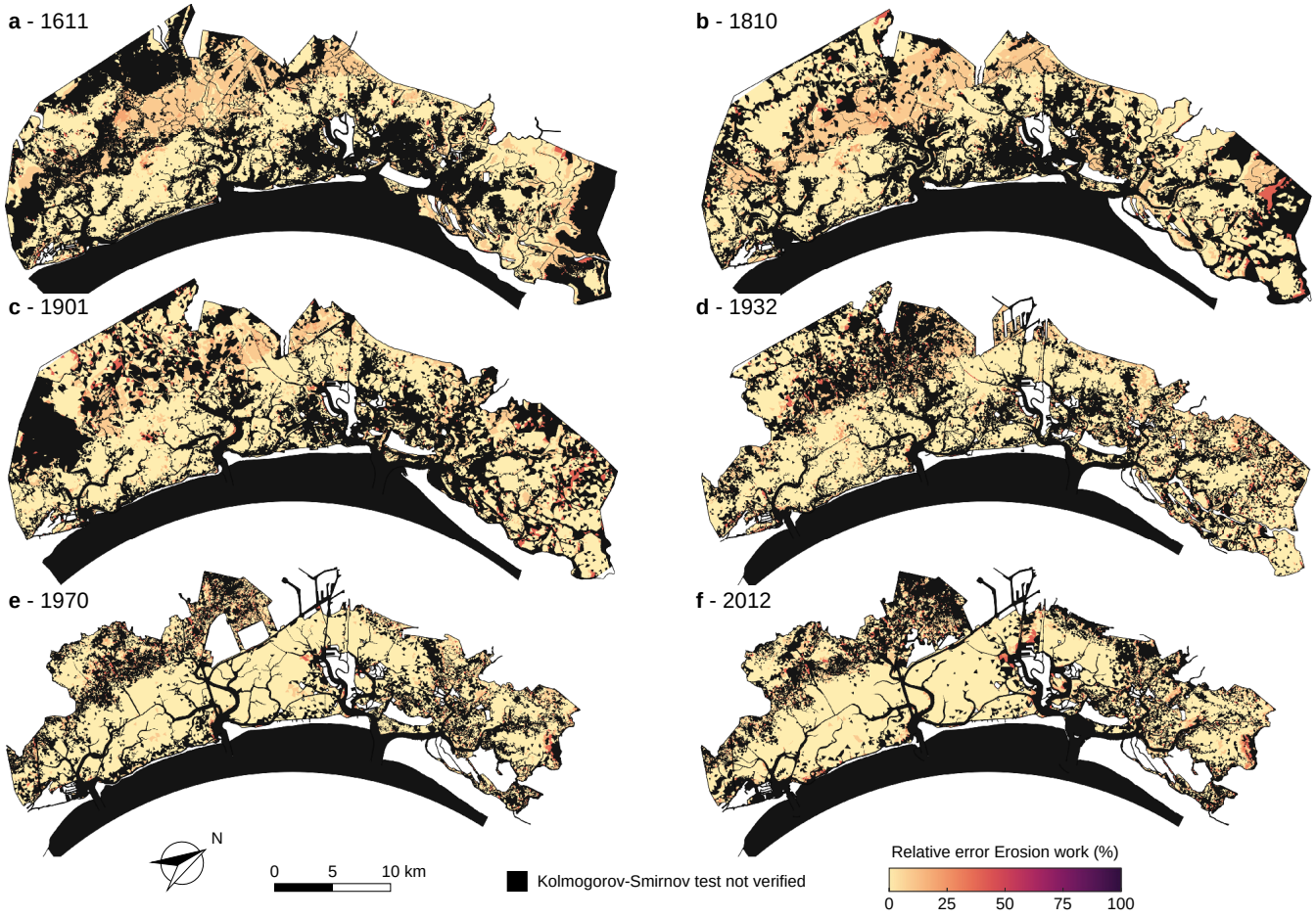

Figure S16. Relative error of synthetic erosion work. Spatial distribution of the relative error between the erosion work calculated with the integral formulation (Eq. 2) and the synthetic one (Eq. 3) for the six different configurations of the Venice Lagoon: (**a**) 1611, (**b**) 1810, (**c**) 1901, (**d**) 1932, (**e**) 1970, and (**f**) 2012. Black identifies sites where the bottom shear stress cannot be modelled as a marked Poisson process (i.e. the KS test is not verified for the interarrival time).

References

Allen, J. I., Somerfield, P. J., and Gilbert, F. J.: Quantifying uncertainty in high-resolution coupled hydrodynamic-ecosystem models, Journal of Marine Systems, 64, 3–14, https://doi.org/10.1016/j.jmarsys.2006.02.010, 2007.

Carniello, L., Defina, A., Fagherazzi, S., and D'Alpaos, L.: A combined wind wave-tidal model for the Venice lagoon, Italy, Journal of Geophysical Research: Earth Surface, 110, 1–15, https://doi.org/10.1029/2004JF000232, 2005.

Carniello, L., D'Alpaos, A., and Defina, A.: Modeling wind waves and tidal flows in shallow micro-tidal basins, Estuarine, Coastal and Shelf Science, 92, 263–276, https://doi.org/10.1016/j.ecss.2011.01.001, 2011.

Defina, A.: Two-dimensional shallow flow equations for partially dry areas, Water Resources Research, 36, 3251–3264, https://doi.org/10.1029/2000WR900167, 2000.

Holthuijsen, L. H., Booij, N., and Herbers, T. H. C.: A prediction model for stationary, short-crested waves in shallow water with ambient currents, Coastal Engineering, 13, 23–54, https://doi.org/https://doi.org/10.1016/0378-3839(89)90031-8, 1989.

Smagorinsky, J.: General circulation experiments with the primitive equations: I. the basic experiment, Monthly Weather Review, 91, 99–164, https://doi.org/10.1175/1520-0493(1963)091<0099:GCEWTP>2.3.CO;2, 1963.